Lattice study on a tetraquark state T_{bb} in the HAL QCD method

Takafumi Aoki,[1,*] Sinya Aoki,[2,3,†] and Takashi Inoue[4,‡]

[1]*Yukawa Institute for Theoretical Physics Kyoto University, Kyoto 606-8502, Japan*
[2]*Center for Gravitational Physics and Quantum Information, Yukawa Institute for Theoretical Physics, Kyoto University, Kyoto 606-8502, Japan*
[3]*RIKEN Nishina Center (RNC), Saitama 351-0198, Japan*
[4]*Nihon University, College of Bioresource Sciences, Kanagawa 252-0880, Japan*

(Received 19 June 2023; accepted 9 August 2023; published 11 September 2023)

We study a doubly bottomed tetraquark state $(bb\bar{u}\,\bar{d})$ with quantum number $I(J^P) = 0(1^+)$, denoted by T_{bb}, in lattice QCD with the nonrelativistic QCD (NRQCD) quark action for b quarks. Employing $(2+1)$-flavor gauge configurations at $a \approx 0.09$ fm on $32^3 \times 64$ lattices, we have extracted the coupled-channel potential between $\bar{B}\bar{B}^*$ and $\bar{B}^*\bar{B}^*$ in the HAL QCD method, which predicts an existence of a bound T_{bb} below the $\bar{B}\bar{B}^*$ threshold. By extrapolating results at $m_\pi \approx 410$, 570, 700 MeV to the physical pion mass $m_\pi \approx 140$ MeV, we obtain a binding energy with its statistical error as $E^{(\mathrm{single})}_{\mathrm{binding}} = 155(17)$ MeV and $E^{(\mathrm{coupled})}_{\mathrm{binding}} = 83(10)$ MeV, where "coupled" means that effects due to virtual $\bar{B}^*\bar{B}^*$ states are included through the coupled channel potential, while only a potential for a single $\bar{B}\bar{B}^*$ channel is used in the analysis for "single." A comparison shows that the effect from virtual $\bar{B}^*\bar{B}^*$ states is quite sizable to the binding energy of T_{bb}. We estimate systematic errors to be ± 20 MeV at most, which are mainly caused by the NRQCD approximation for b quarks.

DOI: 10.1103/PhysRevD.108.054502

I. INTRODUCTION

One of typical characteristic features of QCD is the color confinement that only color-singlet states can appear in nature. While almost all observed color-singlets states are either mesons $(q\bar{q})$ or baryons (qqq), other color-singlet states such as tetraquark state $(qq\bar{q}\,\bar{q})$, pentaquark states $(qqqq\bar{q})$, and glueball states are theoretically allowed to exist. These states are rarely observed and called exotic hadrons, whose existences have not been firmly established yet. Recently, experimental observations have been reported for several heavy exotic hadrons, which include tetraquark states $X(2900)$ [1] and T_{cc} [2] containing one or two charm quarks, a pentaquark state P_c [3] containing a charm and anticharm pair, or tetraquark states Z_b [4] containing a bottom and antibottom pair. Their properties such as particle contents and internal structures, however, are needed to be understood, in particular, theoretically in terms of QCD.

In this paper, as the first step to understand such heavy exotic hadrons, we investigate a tetraquark hadron $(bb\bar{u}\bar{d})$ in $I(J^P) = 0(1^+)$ channel, called T_{bb}, from the first principle using lattice QCD. While T_{bb} has not been experimentally observed yet, theoretical predictions by the diquark model [5] and by color magnetic interactions under the static limit [6,7] suggest existences of heavy tetraquark bound states $QQ\bar{q}\bar{q}$. Indeed, as mentioned before, T_{cc}, a charm counterpart to T_{bb}, seems to exist.

There exist several lattice QCD studies for T_{bb} [8–14], all of which conclude that T_{bb} appears as a bound state below the $\bar{B}\bar{B}^*$ threshold, where the threshold energy is given by $E^{\mathrm{threshold}}_{\bar{B}\bar{B}^*} \simeq 10.604$ GeV. Lattice QCD calculations so far are classified into two categories depending on a treatment of heavy-b quarks. In one approach, b quarks are treated by the static-quark approximation, and the corresponding static-quark potentials have been evaluated. One then solve the Schrödinger equation with the static quark potentials to obtain the binding energy of T_{bb}. The results, however, depends on a number of channels included in the analysis, as shown in Table I. The binding energy in a coupled $\mathcal{B}$ and $\mathcal{B}^*$ channel analysis is 59 MeV [9], which is smaller than 90 MeV of a single $\mathcal{B}$ channel analysis [8] by about 30 MeV, where the $\bar{B}\bar{B}^*$ channel is denoted by $\mathcal{B}$ while the $\bar{B}^*\bar{B}^*$ channel by $\mathcal{B}^*$, whose threshold energy

*takafumi.aoki@yukawa.kyoto-u.ac.jp
†saoki@yukawa.kyoto-u.ac.jp
‡inoue.takashi@nihon-u.ac.jp

TABLE I. Binding energies extrapolated to the physical pion mass in previous lattice studies.

b quark	Analysis	Binding energy of T_{bb} [MeV]
Static approximation	Single $\mathcal{B}$	$90(^{+43}_{-36})$ [8]
	Coupled $\mathcal{B}$ and $\mathcal{B}^*$	$59(^{+30}_{-38})$ [9]
NRQCD approximation	Direct (spectrum)	180(10)(3) [10]
		165(33) [11]
		128(24)(10) [12]
		186(22) [13]
		112(13) [14]

$E^{\text{threshold}}_{\bar{B}^*\bar{B}^*} \simeq 10.649$ GeV is about 45 MeV above the $\bar{B}\bar{B}^*$ threshold. In the other approach, b quarks are treated by the lattice NRQCD, which allows b quarks to move, not only in time but also in space, and one directly evaluate the binding energy of T_{bb} from the corresponding correlation functions. As shown in Table I, the binding energy of T_{bb} in the direct calculations with the NRQCD, ranging from 112 MeV to 186 MeV, are somewhat larger than results from the static quark, 59 MeV or 90 MeV.

One may wonder whether this difference is real beyond statistical and systematic errors except the treatment of b quarks, and if so, what causes the difference. In order to try answering these questions, we calculate the binding energy of T_{bb} in this paper, combining the NRQCD action for b quarks with the couple channel extension of the HAL QCD method [15], which makes it possible to extract the coupled channel potentials directly without assumptions, unlike the finite-volume method [16].

After this introduction, we review the HAL QCD method in Sec. II and summarize our lattice QCD setup, including the NRQCD action for b quarks in Sec. III. In Sec. IV, we present results of potentials and the scattering analysis. Finally we give a summary of this study in Sec. V.

II. HAL QCD METHOD

A. Definition of the potential

A basic quantity for a definition of potentials in the HAL QCD method is the Euclidean time Nambu-Bethe-Salpeter (NBS) wave function, defined by [15,17–19]

$$\begin{aligned}\psi_W^{H_1+H_2}(\mathbf{r},t) &\equiv \psi_W^{H_1+H_2}(\mathbf{r})e^{-Wt} \\ &\equiv \frac{1}{\sqrt{Z_{H_1}}}\frac{1}{\sqrt{Z_{H_2}}}\sum_{\mathbf{x}}\langle\Omega|H_1(\mathbf{x}+\mathbf{r},t)H_2(\mathbf{x},t)| \\ &\quad\times(H_1+H_2);W\rangle, \end{aligned} \tag{1}$$

where $H_i(\mathbf{x},t)$ is the hadron operator at $(\mathbf{x},t)$, $|\Omega\rangle$ is the QCD vacuum state, $|(H_1+H_2);W\rangle$ stands for an eigenstate of the QCD Hamiltonian having quantum numbers of the two-hadrons H_1+H_2 with a center-of-mass energy W, and $Z_{H_i}=|\langle\Omega|H_i(0)|H_i\rangle|^2$ with $|H_i\rangle$ being a single-hadron state. We focus our attention on an energy region below inelastic threshold, where only elastic-scattering occurs. In this energy region, the asymptotic behavior of the ℓth partial wave of the NBS wave function reads

$$\psi_{W,\ell}^{H_1+H_2}(\mathbf{r})\xrightarrow{r\to\infty}[j_\ell(p_W r)-\pi t_\ell(W)h_\ell^+(p_W r)]P_\ell(\hat{\mathbf{r}}\cdot\hat{\mathbf{p}}_W), \tag{2}$$

where the magnitude of the relative momentum p_W is determined from a relation $W=E_{W1}+E_{W2}=\sqrt{p_W^2+m_{H_1}^2}+\sqrt{p_W^2+m_{H_2}^2}$, $P_\ell(z)$ is the Legendre polynomial, $j_\ell(z)/n_\ell(z)$ is the spherical Bessel/Neumann function, and $h_\ell^\pm(z)=n_\ell(z)\pm i j_\ell(z)$ are spherical Hankel functions. The scattering T-matrix $t_\ell(W)$ in the above is related to the unitary S-matrix as $s_\ell(W)=1\text{–}2\pi i t_\ell(W)$, and to the scattering amplitude as $f_\ell(W)=-\frac{\pi}{p_W}t_\ell(W)$.

A hadronic 4-point correlation function in lattice QCD can be expressed in terms of NBS wave functions as

$$\begin{aligned}F_{\mathcal{J}}^{H_1+H_2}(\mathbf{r},t) &\equiv \sum_{\mathbf{x}}\langle\Omega|H_1(\mathbf{x}+\mathbf{r},t)H_2(\mathbf{x},t)\mathcal{J}^\dagger_{H_1+H_2}(t=0)|\Omega\rangle \\ &= \sum_{\mathbf{x}}\sum_n\langle\Omega|H_1(\mathbf{x}+\mathbf{r},t)H_2(\mathbf{x},t)|(H_1+H_2);W_n\rangle\langle(H_1+H_2);W_n|\mathcal{J}^\dagger_{H_1+H_2}(0)|\Omega\rangle+(\text{inela}) \\ &\simeq \sum_n\mathcal{A}_{\mathcal{J},n}\psi_{W_n}^{H_1+H_2}(\mathbf{r},t\geq t^{(\text{inela})}) \xrightarrow{t\to\infty} \mathcal{A}_{\mathcal{J},0}\psi_{W_0}^{H_1+H_2}(\mathbf{r})e^{-W_0 t},\end{aligned} \tag{3}$$

where $\mathcal{J}^\dagger_{H_1+H_2}(0)$ is a source operator which creates two-hadron states at $t=0$ with a target quantum number $I(J^P)$ of H_1+H_2, (inela) represents inelastic contributions, which become negligible at $t\geq t^{(\text{inela})}$, W_0 is the lowest eigenenergy of two hadrons, and

$$\mathcal{A}_{\mathcal{J},n}\equiv\sqrt{Z_{H_1}}\sqrt{Z_{H_2}}\langle(H_1+H_2);W_n|\mathcal{J}^\dagger_{H_1+H_2}(0)|\Omega\rangle. \tag{4}$$

In the HAL QCD method, a nonlocal but energy-independent potential $U(\mathbf{r},\mathbf{r}')$ is formally defined from the NBS wave function so as to satisfy the Schrödinger equation below inelastic threshold as

$$\left(\frac{\nabla^2}{2\mu}+\frac{p_W^2}{2\mu}\right)\psi_W(\mathbf{r})=\int \mathrm{d}^3\mathbf{r}'U(\mathbf{r},\mathbf{r}')\psi_W(\mathbf{r}'), \tag{5}$$

where μ is the reduced mass of two hadrons. Since QCD interactions are short-ranged, $U(\mathbf{r},\mathbf{r}')$ vanishes sufficiently fast as $|\mathbf{r}|$ increases. The potential $U(\mathbf{r},\mathbf{r}')$ may depend on how sink hadron operators H_1 and H_2 are constructed from quarks. Even though a choice of hadron operators is fixed, however, the above equation can not determine $U(\mathbf{r},\mathbf{r}')$ uniquely due to a restriction of the energy below the inelastic threshold [20,21]. Thus, the above definition of the potential is rather formal. For concreteness, we define $U(\mathbf{r},\mathbf{r}')$ in the derivative expansion, which is symbolically written as

$$U(\mathbf{r},\mathbf{r}') = V(\mathbf{r},\nabla)\delta(\mathbf{r}-\mathbf{r}') = \sum_{k=0}^{\infty} V^{(k)}(\mathbf{r})\nabla^k\delta(\mathbf{r}-\mathbf{r}'), \tag{6}$$

and determine coefficient functions $V^{(k)}(\mathbf{r})$ order by order. For example, the leading-order (LO) term can be approximately obtained as

$$V^{(0)}(\mathbf{r};W) = \frac{1}{\psi_W(\mathbf{r})}\left(\frac{\nabla^2}{2\mu}+\frac{p_W^2}{2\mu}\right)\psi_W(\mathbf{r}), \tag{7}$$

where $V^{(0)}(\mathbf{r};W)$, obtained from the NBS wave function $\psi_W(\mathbf{r})$, is the LO approximation of $V^{(0)}(\mathbf{r})$. Given the relationship between the hadron 4-point correlation function and the NBS wave function, the LO potential from the ground state is extracted as

$$V^{(0)}(\mathbf{r};W_0) \simeq \frac{1}{F_{\mathcal{J}}^{H_1+H_2}(\mathbf{r},t)}\left(\frac{\nabla^2}{2\mu}+\frac{p_{W_0}^2}{2\mu}\right)F_{\mathcal{J}}^{H_1+H_2}(\mathbf{r},t), \tag{8}$$

where t should be taken as large as possible to make the lowest-energy state dominate in the 4-point correlation function.

B. Time-dependent method

In order to achieve the ground state saturation in Eq. (8), t should satisfy $t \gg 1/(W_1 - W_0) \propto L^2$ for two-hadron systems, where L is a size of the spatial extension. Since the 4-point function $F_{\mathcal{J}}^{H_1+H_2}(\mathbf{r},t)$ becomes very noisy at such large t, in particular for two-baryon systems, it is impractical to employ Eq. (8) for reliable extractions of potentials. An improved method of extracting the potential that does not require the ground-state saturation has been proposed in Ref. [22], and is employed in this study.

In the improved method, the potential can be extracted directly from a normalized 4-point function, called a R-correlator, which is a sum of NBS wave functions as

$$R_{\mathcal{J}}^{H_1+H_2}(\mathbf{r},t) \equiv \frac{F_{\mathcal{J}}^{H_1+H_2}(\mathbf{r},t)}{e^{-m_{H_1}t}e^{-m_{H_2}t}} \simeq \sum_n \mathcal{A}_{\mathcal{J},n}\psi_{W_n}^{H_1+H_2}(\mathbf{r})e^{-\Delta W_n t}, \tag{9}$$

where we take moderately large $t > t_{\mathrm{threshold}}^{(\mathrm{inela})}$ in the right-hand side, in order suppress inelastic contributions, and $\Delta W_n \equiv W_n - m_{H_1} - m_{H_2}$ satisfies

$$\frac{p_n^2}{2\mu} = \Delta W_n + \frac{1+3\delta^2}{8\mu}(\Delta W_n)^2 + \mathcal{O}((\Delta W_n)^3), \qquad \delta \equiv \frac{|m_{H_1}-m_{H_2}|}{m_{H_1}+m_{H_2}}. \tag{10}$$

Using this relation and taking $t > t_{\mathrm{threshold}}^{(\mathrm{inela})}$, we obtain

$$\begin{aligned}\int d^3\mathbf{r}' U(\mathbf{r},\mathbf{r}')R_{\mathcal{J}}^{H_1+H_2}(\mathbf{r}',t) &\simeq \sum_n \left(\frac{\nabla^2}{2\mu}+\frac{p_n^2}{2\mu}\right)A_n^{\mathcal{J}}\psi_{W_n}^{H_1+H_2}(\mathbf{r})e^{-\Delta W_n t} \\ &\simeq \sum_n \left(\frac{\nabla^2}{2\mu}+\Delta W_n+\frac{1+3\delta^2}{8\mu}(\Delta W_n)^2\right) \times A_n^{\mathcal{J}}\psi_{W_n}^{H_1+H_2}(\mathbf{r})e^{-\Delta W_n t} \\ &= \left(\frac{\nabla^2}{2\mu}-\frac{\partial}{\partial t}+\frac{1+3\delta^2}{8\mu}\frac{\partial^2}{\partial t^2}\right)R_{\mathcal{J}}^{H_1+H_2}(\mathbf{r},t),\end{aligned} \tag{11}$$

which looks like a time-dependent Schrödinger equation for a nonlocal potential with relativistic corrections. It is important to note that potentials can be extracted from a sum of NBS wave functions without knowing individual energy ΔW_n and coefficient $A_n^{\mathcal{J}}$ by this method. At leading order in the derivative expansion, Eq. (11) gives

$$V^{(0)}(\mathbf{r}) = \frac{1}{R_{\mathcal{J}}^{H_1+H_2}(\mathbf{r},t)}\left(\frac{\nabla^2}{2\mu}-\frac{\partial}{\partial t}+\frac{1+3\delta^2}{8\mu}\frac{\partial^2}{\partial t^2}\right) \times R_{\mathcal{J}}^{H_1+H_2}(\mathbf{r},t), \tag{12}$$

where a t-dependence in the right-hand side is canceled between numerator and denominator if inelastic contributions become negligible at $t > t_{\mathrm{threshold}}^{(\mathrm{inela})}$. In practice, we use the t-independence of $V^{(0)}(\mathbf{r})$ as an indicator for $t > t_{\mathrm{threshold}}^{(\mathrm{inela})}$ to satisfy.

C. Coupled-channel HAL QCD method

Since thresholds of $\mathcal{B}(\bar{B}+\bar{B}^*)$ and $\mathcal{B}^*(\bar{B}^*+\bar{B}^*)$ are so close, we can not ignore an influence of the $\mathcal{B}^*$ channel to a potential in the $\mathcal{B}$ channel. We thus decided to employ the coupled channel extension of the HAL QCD method in our study.

To explain this extension, we consider an energy region where an inelastic scattering $A+B\to C+D$ in addition to an elastic-scattering $A+B\to A+B$ occurs with $m_A+m_B<m_C+m_D$. The NBS wave function of the scattering channel $\alpha=0,1$ is denoted by

$$\psi^\alpha_{W;\beta}(\mathbf{r},t)\equiv\psi^\alpha_{W;\beta}(\mathbf{r})e^{-Wt} \equiv\frac{1}{\sqrt{Z^\alpha_1}\sqrt{Z^\alpha_2}}\sum_{\mathbf{x}}\langle\Omega|H^\alpha_1(\mathbf{x}+\mathbf{r},t)H^\alpha_2(\mathbf{x},t)|W;\beta\rangle, \tag{13}$$

where $(H^0_1,H^0_2)=(A,B)$ or $(H^1_1,H^1_2)=(C,D)$, and W is the center-of-mass energy. At a given energy W, there exists two independent states with the same quantum number as $A+B$, labeled by β, which are expanded in terms of asymptotic states as $|W;\beta\rangle=c^{0\beta}|A+B;W\rangle+c^{1\beta}|C+D;W\rangle+\cdots$. Thus, as in the case of the elastic scattering, an asymptotic behavior of an ℓth partial wave of the NBS wave function reads [20]

$$\psi^\alpha_{W;\beta,\ell}(\mathbf{r})\xrightarrow{r\to\infty}\sum_\gamma[\delta^{\alpha\gamma}j_\ell(p^\alpha_W r)+p^\alpha_W h^+_\ell(p^\alpha_W r)f^{\alpha\gamma}_\ell(W)] \times c^{\gamma\beta}P_\ell(\hat{\mathbf{r}}\cdot\hat{\mathbf{p}}^\alpha_W), \tag{14}$$

where the scattering amplitude from a channel γ to a channel α is defined from the T matrix $t^{\alpha\gamma}_\ell$ as

$$f^{\alpha\gamma}_\ell(W)\equiv-\pi\sqrt{\frac{E^\alpha_{W1}E^\alpha_{W2}}{E^\gamma_{W1}E^\gamma_{W2}}}\sqrt{\frac{1}{p^\alpha_W p^\gamma_W}}t^{\alpha\gamma}_\ell(W). \tag{15}$$

Since Eq. (14) is identical to an asymptotic solution to a coupled-channel Schrödinger equation with the total energy W [23], we define the coupled-channel potential as

$$\left(\frac{\nabla^2}{2\mu^\alpha}+\frac{(p^\alpha_W)^2}{2\mu^\alpha}\right)\psi^\alpha_{W;\beta}(\mathbf{r})\equiv\sum_\gamma\int\mathrm{d}^3\mathbf{r}'U^{\alpha\gamma}(\mathbf{r},\mathbf{r}')\psi^\gamma_{W;\beta}(\mathbf{r}'), \tag{16}$$

where p^α_W and μ^α are a magnitude of the relative momentum and a reduced mass in the channel α, respectively.

As in Eq. (6) for the single channel case, the nonlocal potential $U^{\alpha\beta}(\mathbf{r},\mathbf{r}')$ is defined in term of the derivative expansion, whose leading-order term is given by

$$U^{\alpha\gamma}(\mathbf{r},\mathbf{r}')=V^{\alpha\gamma}(\mathbf{r})\delta(\mathbf{r}-\mathbf{r}')+\mathcal{O}(\nabla). \tag{17}$$

The LO potential can be approximately extracted from two NBS wave functions by a matrix inversion as

$$\begin{pmatrix}V^{00}(\mathbf{r}) & V^{01}(\mathbf{r})\\ V^{10}(\mathbf{r}) & V^{11}(\mathbf{r})\end{pmatrix} =\begin{pmatrix}K^0_{W_0;\beta_0}(\mathbf{r}) & K^0_{W_1;\beta_1}(\mathbf{r})\\ K^1_{W_0;\beta_0}(\mathbf{r}) & K^1_{W_1;\beta_1}(\mathbf{r})\end{pmatrix}\begin{pmatrix}\psi^0_{W_0;\beta_0}(\mathbf{r}) & \psi^0_{W_1;\beta_1}(\mathbf{r})\\ \psi^1_{W_0;\beta_0}(\mathbf{r}) & \psi^1_{W_1;\beta_1}(\mathbf{r})\end{pmatrix}^{-1}, \tag{18}$$

where $K^\alpha_{W;\beta}(\mathbf{r})$ is given by the left-hand side of Eq. (16). For the matrix inversion to obtain potentials, we must take two linearly-independent NBS wave functions, by choosing W and β appropriately. Note that it is not guaranteed that the coupled channel potential is Hermitian due to the approximation of the derivative expansion.

As in the case of the single channel, the coupled channel 4-point function is expressed in terms of NBS wave functions as

$$F^\alpha_\xi(\mathbf{r},t)=\sum_{\mathbf{x}}\langle\Omega|H^\alpha_1(\mathbf{x}+\mathbf{r},t)H^\alpha_2(\mathbf{x},t)\mathcal{J}^\dagger_\xi(t=0)|\Omega\rangle \xrightarrow{t\to\infty}\sqrt{Z^\alpha_1}\sqrt{Z^\alpha_2}\sum_{i=0,1}\psi^\alpha_{W_i}(\mathbf{r})\mathcal{A}_{W_i;\xi}e^{-W_it},$$
$$\mathcal{A}_{W_i;\xi}\equiv\langle W_i|\mathcal{J}^\dagger_\xi(0)|\Omega\rangle, \tag{19}$$

where W_0 and W_1 are lowest two energies of this coupled-channel system. To extract the 2×2 potential matrix, we need to determine $\mathcal{A}_{W_{0,1};\xi}$ for two linearly independent $J^\dagger_\xi$, as well as $W_{0,1}$.

The R-correlator in the channel α, defined by

$$R^\alpha_\xi(\mathbf{r},t)\equiv\frac{F^\alpha_\xi(\mathbf{r},t)}{e^{-m^\alpha_1t}e^{-m^\alpha_2t}}\simeq\sum_{n,\beta}\mathcal{A}^\alpha_{W_n;\beta,\xi}\psi^\alpha_{W_n;\beta}(\mathbf{r})e^{-\Delta^\alpha W_{\xi,n}t}, \tag{20}$$

where we take $t>t^{(\mathrm{inela})}_{\mathrm{threshold}}$ in the right-hand side with $\Delta^\alpha W_{\xi,n}\equiv W_{\xi,n}-m^\alpha_1-m^\alpha_2$, satisfies

$$\left(\frac{\nabla^2}{2\mu^\alpha}-\frac{\partial}{\partial t}+\frac{1+3\delta^{\alpha2}}{8\mu^\alpha}\frac{\partial^2}{\partial t^2}\right)R^\alpha_\xi(\mathbf{r},t) \simeq\sum_\beta\tilde{\Delta}^{\alpha\beta}(t)\int\mathrm{d}^3\mathbf{r}'U^{\alpha\beta}(\mathbf{r},\mathbf{r}')R^\beta_\xi(\mathbf{r}',t) \tag{21}$$

up to $\mathcal{O}((\Delta W)^2)$ as in the single-channel case, where

$$\tilde{\Delta}^{\alpha\beta}(t)=\sqrt{\frac{Z^\beta_1Z^\beta_2}{Z^\alpha_1Z^\alpha_2}}\frac{\mathrm{e}^{-(m^\beta_1+m^\beta_2)t}}{\mathrm{e}^{-(m^\alpha_1+m^\alpha_2)t}}, \tag{22}$$

which is needed to correct differences in masses and Z-factors between two channels. Denoting the left-hand side of Eq. (21) as $\mathcal{K}^\alpha_\xi(\mathbf{r},t)$, the LO potential is extracted as

$$\begin{pmatrix} V^{00}(\mathbf{r}) & \tilde{\Delta}^{01}(t)V^{01}(\mathbf{r}) \\ \tilde{\Delta}^{10}(t)V^{10}(\mathbf{r}) & V^{11}(\mathbf{r}) \end{pmatrix} = \begin{pmatrix} \mathcal{K}_0^0(\mathbf{r},t) & \mathcal{K}_1^0(\mathbf{r},t) \\ \mathcal{K}_0^1(\mathbf{r},t) & \mathcal{K}_1^1(\mathbf{r},t) \end{pmatrix} \begin{pmatrix} R_0^0(\mathbf{r},t) & R_1^0(\mathbf{r},t) \\ R_0^1(\mathbf{r},t) & R_1^1(\mathbf{r},t) \end{pmatrix}^{-1}. \tag{23}$$

As before, there is no guarantee that the LO potential is Hermitian.

III. LATTICE QCD SETUP

A. Operators

We are interested in the doubly bottomed tetraquark state with quantum numbers $I(J^P) = 0(1^+)$, called T_{bb} hereafter. The lowest scattering channel with these quantum numbers is the $\mathcal{B}$ ($\bar{B}\bar{B}^*$) channel with threshold near 10600 MeV, while the second one is the $\mathcal{B}^* \equiv (\bar{B}^*\bar{B}^*)$ channel with a threshold at 45 MeV above [24]. Since the threshold of the third channel is too far above to contribute low-energy states such as T_{bb}, we only consider $\mathcal{B}$ and $\mathcal{B}^*$ channels in this paper.

Sink operators for two mesons at a distance $\mathbf{r}$ with a total spin $S = 1$ and a total isospin $I = 0$ are taken as

$$\mathcal{B}_j \equiv \sum_{\mathbf{x}} \underbrace{(\bar{u}(\mathbf{y})\gamma_5 b(\mathbf{y}))}_{\bar{B}(\mathbf{y})} \underbrace{(\bar{d}(\mathbf{x})\gamma_j b(\mathbf{x}))}_{\bar{B}^*(\mathbf{x})} - [u \leftrightarrow d], \quad \mathbf{y} \equiv \mathbf{x} + \mathbf{r}, \tag{24}$$

$$\mathcal{B}_j^* \equiv \epsilon_{jkl} \sum_{\mathbf{x}} (\bar{u}(\mathbf{y})\gamma_k b(\mathbf{y}))(\bar{d}(\mathbf{x})\gamma_l b(\mathbf{x})) - [u \leftrightarrow d], \tag{25}$$

where j, k, l are spatial vector indices. At the source, interchanges between $q \leftrightarrow \bar{q}$ are made for $q = u$, d, b, together with uses of wall sources for $q = u$, d.

In addition to these two meson operators, we introduce an operator made of two diquarks, called $\mathcal{D}$, at the source as

$$\mathcal{D}_j^\dagger \equiv (\epsilon^{abc}\bar{b}^b(s_0)\gamma_j C\bar{b}^c(s_0))(\epsilon^{ade}d^d(s_0)C\gamma_5 u^e(s_0)) - [u \leftrightarrow d], \tag{26}$$

where $a, b, c, \ldots$ denote color indices, $C = \gamma_4\gamma_2$ is the charge-conjugation matrix, and the argument s_0 in the quark field denotes a source point [12].

A reason for a use of the diquark at the source is as follows. If we perform a coupled-channel analysis with $\mathcal{B}^\dagger$ and $\mathcal{B}^{*\dagger}$ source operators, an inverse matrix in Eqs. (18) or (23) becomes singular, probably because $\mathcal{B}^\dagger$ and $\mathcal{B}^{*\dagger}$ source operators create similar combinations of states, a meson-meson state (primary) plus a compact state (secondly), as seen in Fig. 5 of Ref. [12]. To overcome this difficulty, we introduce the diquark-type source $\mathcal{D}^\dagger$, which probably couples to a different combination of states. We then perform the coupled-channel analysis for the R-correlators (or the NBS wave functions) with $\mathcal{B}$ and $\mathcal{B}^*$ as sink operators, and $\mathcal{B}^\dagger$ and $\mathcal{D}^\dagger$ as source operators, which leads to more stable results than $\mathcal{B}^{*\dagger}$ and $\mathcal{D}^\dagger$ sources.

B. Light-quark propagators

In this work, we impose exact isospin symmetry on u, d quarks, so that propagators for both quarks are identical. In our study, we employ the Wilson-Clover operator for the quark, given by

$$D(x|y) = \delta_{x,y} - \kappa \sum_\mu \{(1-\gamma_\mu)U_\mu(x)\delta_{x+\hat{\mu},y} + (1+\gamma_\mu)U_\mu^\dagger(x-\hat{\mu})\delta_{x-\hat{\mu},y}\} - \kappa c_{\mathrm{sw}} \frac{1}{2} \sum_{\mu,\nu} \frac{[\gamma_\mu, \gamma_\nu][\Delta_\mu, \Delta_\nu]}{2}, \tag{27}$$

where Δ_μ in the clover term are symmetric covariant difference operator, defined by

$$\Delta_\mu f(x) = U_\mu(x)f(x+\hat{\mu}) - U_\mu^\dagger(x-\hat{\mu})f(x-\hat{\mu}), \tag{28}$$

and $\hat{\mu}$ is a unit vector in the μ direction with a length a, where a is a lattice spacing. See Sec. III D for parameters κ, c_{sw} used in this study. As mentioned before, we use wall sources for light quarks.

C. Heavy-quark propagator

As long as the relativistic lattice fermion is used, $am_Q \ll 1$ is required to keep lattice artifact small, where m_Q is a quark mass. This condition, however, is badly violated for the b quark in our simulations, since $m_b \approx 4.2$ GeV and $a \approx 0.09$ fm ($1/a \simeq 2$ GeV). Therefore, we cannot treat the b quark relativistically on a lattice. Fortunately, since the typical velocity of the b quark inside a hadron is $v^2 \sim 0.1$ [25], and thus sufficiently nonrelativistic, we can treat the b quark in the nonrelativistic QCD (NRQCD) approximation. The NRQCD approximation improves the static approximation, by including effects of moving b quarks in space, which seem to give a non-negligible contribution to the binding energy of the tetraquark state [8,12].

In the NRQCD, we evaluate a time evolution of the heavy-quark propagator according to nonrelativistic dynamics using a Hamiltonian without b-quark mass term. The NRQCD Hamiltonian at the tree level is obtained from the QCD Hamiltonian by the Foldy-Wouthuysen-Tani (FWT) transformation [26,27] designed to be block diagonal up to $\mathcal{O}(v^n)$ in spinor space as

$$\mathcal{H}_{\mathrm{QCD}} \to \mathcal{R}\mathcal{H}_{\mathrm{NRQCD}}\mathcal{R}^\dagger \simeq \mathcal{R}\begin{pmatrix} \mathcal{H}_\psi & 0 \\ 0 & \mathcal{H}_{\chi^\dagger} \end{pmatrix}\mathcal{R}^\dagger, \tag{29}$$

where $\mathcal{R}$ is the FWT transformation matrix. The propagator for the particle field ψ moving in the positive direction can be approximated as

$$D^{-1}(x|y) \to \mathcal{R}\overline{\psi(x)\psi^{\dagger}}(y)\mathcal{R}^{\dagger} \simeq \mathcal{R}\begin{pmatrix} G_{\psi}(x|y) & 0 \\ 0 & 0 \end{pmatrix}\mathcal{R}^{\dagger}\theta(x_4 - y_4), \quad (30)$$

and the two-spinor NRQCD propagator G_{ψ} is evolved in time by $\mathcal{H}_{\psi} \equiv \mathcal{H}_0 + \delta\mathcal{H}$ on a lattice as [28]

$$\begin{aligned} G(\mathbf{x}, t+1|s_0) = &\left(1 - \frac{\mathcal{H}_0}{2n}\right)^n \left(1 - \frac{\delta\mathcal{H}}{2}\right) \\ &\times U_4^{\dagger}(x)\left(1 - \frac{\delta\mathcal{H}}{2}\right)\left(1 - \frac{\mathcal{H}_0}{2n}\right)^n G(\mathbf{x}, t|s_0) \\ &+ s_0(\mathbf{x})\delta_{t+1,0}, \end{aligned} \quad (31)$$

where s_0 is a source vector defined previously, and $n = 2$ is a stabilization parameter for numerical calculations. This calculation requires much smaller computational costs than solving linear equations for relativistic quark propagators. In this work, we use the block-diagonal Hamiltonian up to $\mathcal{O}(v^4)$ [29], given on a lattice as

$$\begin{aligned} &\mathcal{H}_{\psi} = \mathcal{H}_0 + \sum_i c_i \delta\mathcal{H}^{(i)}, \qquad \mathcal{H}_0 = -\frac{1}{2M}\Delta^{(2)}, \\ &\delta\mathcal{H}^{(1)} = -\frac{1}{2M}\boldsymbol{\sigma}\cdot\mathbf{B}, \qquad \delta\mathcal{H}^{(2)} = \frac{i}{8M^2}(\Delta\cdot\mathbf{E} - \mathbf{E}\cdot\Delta), \\ &\delta\mathcal{H}^{(3)} = -\frac{1}{8M}\boldsymbol{\sigma}\cdot(\Delta\times\mathbf{E} - \mathbf{E}\times\Delta), \\ &\delta\mathcal{H}^{(4)} = -\frac{1}{8M^3}(\Delta^{(2)})^2, \qquad \delta\mathcal{H}^{(5)} = \frac{1}{24M}\Delta^{(4)}, \\ &\delta\mathcal{H}^{(6)} = -\frac{1}{16nM^2}(\Delta^{(2)})^2, \end{aligned} \quad (32)$$

where M is the bare heavy-particle mass, $c_i = 1$ at the tree level in perturbation theory, $\Delta, \Delta^{(2)}, \ldots$ are discretized symmetric covariant derivatives in space, and the chromoelectromagnetic field $\mathbf{E}, \mathbf{B}$ are given by the standard clover-leaf definitions. The FWT transformation matrix is also given up to $\mathcal{O}(v^4)$ [29] as

$$\begin{aligned} &\mathcal{R} = 1 + \sum_i \mathcal{R}^{(i)}, \\ &\mathcal{R}^{(1)} = -\frac{1}{2M}\gamma\cdot\Delta, \qquad \mathcal{R}^{(2)} = \frac{1}{8M^2}\Delta^{(2)}, \\ &\mathcal{R}^{(3)} = \frac{1}{8M^2}\cdot\mathbf{B}, \qquad \mathcal{R}^{(4)} = -\frac{i}{4M^2}\gamma_4\boldsymbol{\gamma}\cdot\mathbf{E}. \end{aligned} \quad (33)$$

In our study, all link variables are rescaled as $U_{\mu} \to U_{\mu}/u_0$, in order to include perturbative corrections by the tadpole improvement [28], where u_0 is determined from an average of the plaquette U_P as

$$u_0 = \left\{\frac{1}{3}\mathrm{Tr}U_P\right\}^{1/4}. \quad (34)$$

In the lattice NRQCD, the ground-state energy obtained from a behavior of the two-point function in time represents the interaction energy, not the hadron mass itself, since the quark-mass term is removed from the NRQCD Hamiltonian. Therefore, a correlation function with nonzero momentum behaves at large t as

$$\begin{aligned} &\langle H_X(\mathbf{p}, t)H_X^{\dagger}(\mathbf{p}, 0)\rangle \xrightarrow{t\to\infty} e^{-E_X(\mathbf{p})t}, \\ &H_X(\mathbf{p}) \equiv \sum_{\mathbf{x}} H_X(\mathbf{x})e^{-i\mathbf{p}\mathbf{x}}, \end{aligned} \quad (35)$$

where $E_X(\mathbf{p}) = \sqrt{\mathbf{p}^2 + (M_X^{\mathrm{kin}})^2} - \delta$ with the $\mathbf{p}$ independent energy shift δ. Since this energy shift δ, equal to the bare quark mass at the tree level, usually suffers from large perturbative corrections, we directly estimate a (kinetic) mass of the hadron X without determining δ as

$$M_X^{\mathrm{kin}} = \frac{\mathbf{p}^2 - (E_X(\mathbf{p}) - E_X(\mathbf{0}))^2}{2(E_X(\mathbf{p}) - E_X(\mathbf{0}))}. \quad (36)$$

D. Configurations

We have employed the $(2+1)$-flavor full QCD configurations, generated by the PACS-CS Collaboration [30] with the Iwasaki gauge action and the Wilson-Clover light-quark action at $a \approx 0.09$ fm. For the wall source, gauge configurations are fixed to the Coulomb gauge. We estimate statistical errors by the jackknife method, with a bin size 20, using 400 configurations on each quark mass. Parameters for gauge ensembles and hadron masses measured in this work are listed in Tables II and III, respectively.

Comments on measured hadron masses are in order:

(i) While an individual mass of $\bar{B}$ or $\bar{B}^*$ has a sizable statistical error due to a use of data at nonzero $\mathbf{p}$ in Eq. (36), we can determine the mass splitting between them from $E_{\bar{B}^*}(\mathbf{0}) - E_{\bar{B}}(\mathbf{0})$, which does not require noisy data at nonzero $\mathbf{p}$. In the table, we also list the spin average mass $M_{\bar{B}}^{\mathrm{spinavg}} \equiv \frac{1}{4}M_{\bar{B}} + \frac{3}{4}M_{\bar{B}^*}$. For calculations of potentials, we need to use $M_{\bar{B}}$ and $M_{\bar{B}^*}$ separately.

(ii) Values of $\bar{B}$ meson mass in the table are consistent with an experimental value $M_{\bar{B}}^{\mathrm{spinavg}} = 5313$ MeV [24] within large statistical errors at three light-quark masses, and we expect that this agreement holds even at the physical pion mass. Thanks to smaller statistical errors, on the other hand, we observe a tendency that the mass splitting $\Delta E_{\bar{B}\bar{B}^*}$ decreases as the pion mass decreases and it becomes smaller than an experimental value $\Delta E_{\bar{B}\bar{B}^*} = 45$ MeV [24] at the physical pion mass. Among possible reasons for

TABLE II. Parameters for gauge ensembles. The bare b-quark mass M_b is taken to satisfy $M_{b\bar{b}}^{\text{spinavg}} \approx 9450$ MeV within errors. The expectation value of the link variable u_0 defined in Eq. (34) is used for the tadpole improvements.

Configuration	$V_{\text{lat}} = L_s^3 \times L_t$	a (fm)	L_s (fm)	κ_{ud}	κ_s	c_{sw}	M_b	u_0
PACS-CS-A	$32^3 \times 64$	0.0907(13)	2.902(42)	0.13700	0.13640	1.715	1.919	0.868558(42)
PACS-CS-B	$32^3 \times 64$	0.0907(13)	2.902(42)	0.13727	0.13640	1.715	1.919	0.868793(43)
PACS-CS-C	$32^3 \times 64$	0.0907(13)	2.902(42)	0.13754	0.13640	1.715	1.919	0.869005(44)

TABLE III. Hadron masses measured on each ensemble. The B-meson mass $M_{\bar{B}}$ is determined by the kinetic mass, and the spin-averaged mass is $\frac{1}{4}M_{\bar{B}} + \frac{3}{4}M_{\bar{B}^*}$. The energy-splitting $\Delta E_{\bar{B}\bar{B}^*}$ is defined by $\Delta E_{\bar{B}\bar{B}^*} \equiv E_{\bar{B}^*}(\mathbf{0}) - E_{\bar{B}}(\mathbf{0})$.

Configuration	m_π (MeV)	m_ρ (MeV)	$M_{\bar{B}}^{\text{spinavg}}$ (MeV)	$\Delta E_{\bar{B}\bar{B}^*}$ (MeV)
PACS-CS-A	701(1)	1102(1)	5440(174)	49.4(2.6)
PACS-CS-B	571(0)	1011(1)	5382(269)	44.9(1.6)
PACS-CS-C	416(1)	920(3)	5332(220)	42.7(3.9)

this, it is most likely that $c_1 = 1$ with the tadpole improvement is not good enough as a coefficient of $\delta\mathcal{H}^{(1)}$ in the NRQCD Hamiltonian, which is the LO term in the NRQCD power counting responsible for the spin splitting. Therefore we expect 10–20% systematic errors for the spin splittings at the tree-level coefficient even with the tadpole improvement.

In this work, scattering quantities are calculated on three different pion masses, and then extrapolated to the physical point defined by $m_\pi \approx 140$ MeV.

IV. NUMERICAL RESULTS

A. Leading-order potential

1. Single-channel case

In this subsection, assuming that the T_{bb} couples only to the $\mathcal{B}$ channel, we compute the S-wave[1] LO potential according to Eq. (12). Figure 1 (left) shows the one at $m_\pi \simeq 700$ MeV (PACS-CS-A) and $t = 13$. Here and hereafter, t is always given in the lattice unit. The potential between $\bar{B}$ and $\bar{B}^*$ mesons is attractive at all distances and it becomes zero within errors at distances larger than 1.0 fm, which is smaller than $L_s/2 \simeq 1.45$ fm. Thus, the interaction is sufficiently short-ranged to be confined within the box, so that finite size effect to the potential is expected to be small. To fit data of the potential, we use a 3-Gauss function given by

$$V_{3\text{G}}(r) = \mathcal{V}_0 e^{-r^2/\rho_0^2} + \mathcal{V}_1 e^{-r^2/\rho_1^2} + \mathcal{V}_2 e^{-r^2/\rho_2^2}, \quad (37)$$

where $\mathcal{V}_i$ and ρ_i are fit parameters. We show fit results to lattice data at $t = 12$–14 in Fig. 1 (right), whose time dependence is negligibly small, indicating that contaminations from inelastic states are well under control. Thus we have employed the potential at $t = 13$ for our main analysis, whose fit parameters are given in Table IV.

2. Coupled-channel case

We now consider a case that the T_{bb} couples to $\mathcal{B}$ and $\mathcal{B}^*$ channels. In this situation, we compute the S-wave LO potential using Eq. (23). Figure 2 (upper) show 2×2 coupled-channel potentials at $m_\pi \simeq 700$ MeV (PACS-CS-A) and $t = 13$, which become zero within errors at $r \gtrsim 1.0$ fm, together with 3-Gauss fit by red lines. As before, we thus confirm that interactions in this channel are sufficiently short-range, so that possible finite-size effects are expected to be small.

A diagonal potential, $V^{\mathcal{B}\mathcal{B}}$, is attractive at distances smaller than 0.8 fm, while another one, $V^{\mathcal{B}^*\mathcal{B}^*}$, has a repulsive core at short distances surrounded by an attractive pocket at $r \simeq 0.4$ fm. On the other hand, magnitudes of off-diagonal interactions between $\mathcal{B}$ and $\mathcal{B}^*$ channels are comparable to those of diagonal interactions, showing that a channel coupling between $\mathcal{B}$ and $\mathcal{B}^*$ is significant. This observation suggests an importance of a coupled-channel analysis or conversely a possibility that a single-channel analysis may contain large systematic uncertainties. In addition, we have observed that Hermiticity of the 2×2 potential matrix is badly broken; two off-diagonal components are very different. We speculate that the leading-order approximation for the original nonlocal coupled-channel potential, which should be Hermitian, causes this large violation of Hermiticity, suggesting strong nonlocality of the coupled-channel potential in this system, which is consistent with our observation that off-diagonal interactions are significant.

[1]The NBS wave function is projected to the A_1^+ representation of the cubic group, where we ignore higher partial waves such as $\ell = 4, 6, \ldots$.

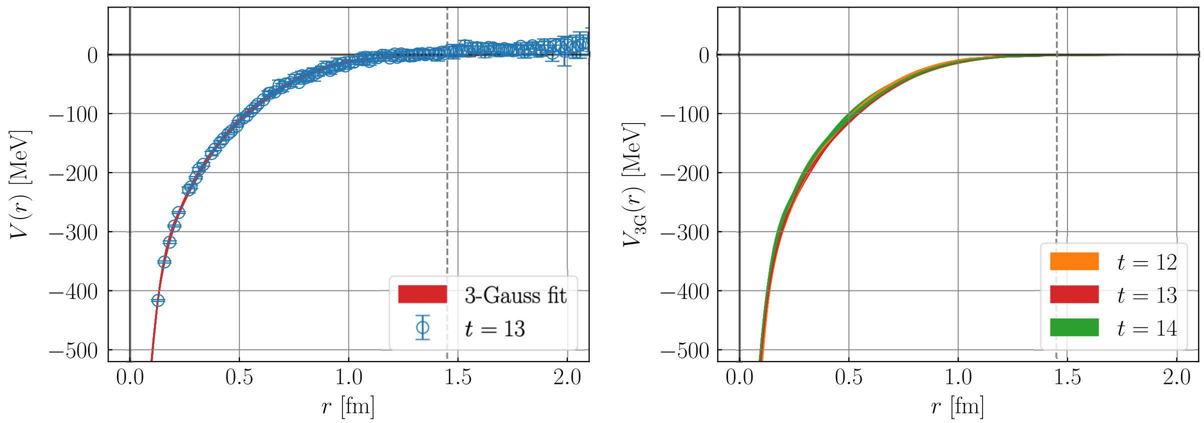

FIG. 1. Left: a lattice result of the potential at $t = 13$ (blue circles), together with the 3-Gauss fit by a red line. Right: 3-Gauss fits at $t = 12, 13, 14$. A gray-dashed line indicates $r = L/2$.

Since the standard scattering analysis requires the unitarity of the S-matrix, which is guaranteed by Hermitian potentials, we can not perform the coupled-channel analysis for scatterings above the $\mathcal{B}^*$ threshold. In this paper, however, we still employ coupled-channel potentials for a scattering analysis in the $\mathcal{B}$ channel below the $\mathcal{B}^*$ threshold, in order to partly incorporate nonlocality caused by off shell $\mathcal{B}^*$ propagations. Details of such an analysis will be given in Sec. IV B.

Figure 2 (lower) presents 3-Gaussian fits to lattice data at $t = 12$–14. An off-diagonal component $V^{\mathcal{B}\mathcal{B}^*}$ show a detectable time dependence at the short distance, which however is found to give tiny effects on scattering quantities. We therefore conclude that contributions from inelastic states are well under control, and we employ $t = 13$ data in our main analysis. Table V gives fit parameters of the coupled channel potential at $t = 13$.

3. *Pion-mass dependence*

Figure 3 compares potentials at three different pion masses, $m_\pi = 701, 571, 416$ MeV. As the pion mass gets smaller, both diagonal and off-diagonal potentials become stronger and more long-range. This suggests that a mixing effect between $\mathcal{B}$ and $\mathcal{B}^*$ increases toward the physical pion mass, so that the coupled-channel analysis may be mandatory even below the $\mathcal{B}^*$ threshold. In this study, physical observables such as scattering phase shifts and a binding energy, not potentials themselves, are extrapolated from results at three heavier pion masses to the physical pion mass, $m_\pi = 140$ MeV.

TABLE IV. 3-Gauss fit parameters at $t = 13$.

V	$\mathcal{V}_i$ (MeV)	ρ_i (fm)
$i = 0$	−482(11)	0.088(0.002)
$i = 1$	−185(8)	0.218(0.004)
$i = 2$	−236(2)	0.583(0.002)

B. Scattering analysis

1. *Inclusion of virtual $\mathcal{B}^*$ effects*

In the following analysis, we restrict ourself to scatterings only in the $\mathcal{B}$ channel below the $\mathcal{B}^*$ threshold, where the $\mathcal{B}^*$ channel virtually appear as intermediate states, even though we employ the 2×2 coupled-channel potential matrix in the analysis. This kind of situation has been analyzed in [20], which shows that effects of virtual $\mathcal{B}^*$ states appear as nonlocality of the effective potential in the $\mathcal{B}$ channel. Explicitly, the coupled channel Schrödinger equation between $\mathcal{B}$ and $\mathcal{B}^*$ becomes an effective single channel Schrödinger equation in the $\mathcal{B}$ channel as

$$(H_0 + U^{\mathcal{B}\mathcal{B}}_{\mathrm{eff},E})\Psi_B = E\Psi_B, \tag{38}$$

where

$$\begin{aligned} U^{\mathcal{B}\mathcal{B}}_{\mathrm{eff},E}(\mathbf{x},\mathbf{y}) &= V^{\mathcal{B}\mathcal{B}}(\mathbf{x})\delta(\mathbf{x}-\mathbf{y}) \\ &\quad + V^{\mathcal{B}\mathcal{B}^*}(\mathbf{x})G^{\mathcal{B}^*\mathcal{B}^*}_E(\mathbf{x},\mathbf{y})V^{\mathcal{B}^*\mathcal{B}}(\mathbf{y}), \end{aligned} \tag{39}$$

where $G^{\alpha\alpha}_E(\mathbf{x},\mathbf{y}) = (E - H^\alpha_0 - V^{\alpha\alpha})^{-1}(\mathbf{x},\mathbf{y})$ is the full Green function for the energy E in the α channel, and thus the effective potential $U^{\mathcal{B}\mathcal{B}}_{\mathrm{eff},E}(\mathbf{x},\mathbf{y})$ explicitly depends on the energy E. In this expression, it is clear that effects of intermediate $\mathcal{B}^*$ states leads to nonlocality for $U^{\mathcal{B}\mathcal{B}}_{\mathrm{eff},E}(\mathbf{x},\mathbf{y})$ in the second term. While the original $U(\mathbf{x},\mathbf{y})$ is defined in QCD, $U^{\mathcal{B}\mathcal{B}}_{\mathrm{eff},E}(\mathbf{x},\mathbf{y})$ contains only a part of nonlocality caused by such intermediate $\mathcal{B}^*$ states with *local* interactions $V^{\mathcal{B}^*\mathcal{B}^*}$, $V^{\mathcal{B}\mathcal{B}^*}$, and $V^{\mathcal{B}^*\mathcal{B}}$ for a given energy E. A remaining nonlocality comes not only from nonlocality of coupled channel potentials but also from virtual channels other than $\mathcal{B}$ and $\mathcal{B}^*$, latter of which have negligible effects on the scattering in the $\mathcal{B}$ channel below the $\mathcal{B}^*$ threshold, since thresholds of other channels are far above from it.

Note that, even though $U^{\mathcal{B}\mathcal{B}}_{\mathrm{eff},E}(\mathbf{x},\mathbf{y})$ is still non-Hermitian, we can extract real-scattering phase shifts in

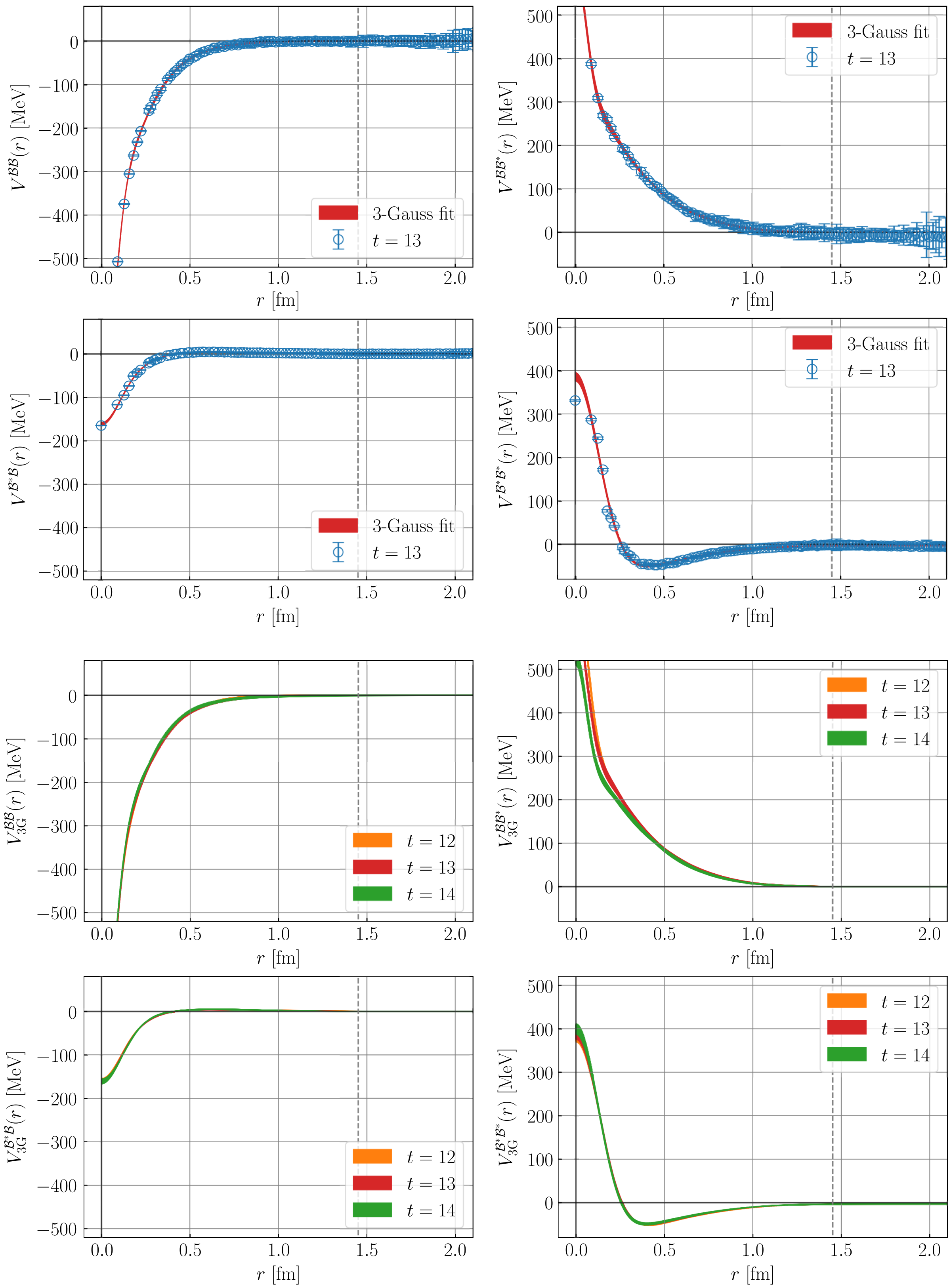

FIG. 2. Upper: 2×2 coupled-channel potentials (blue circles) at $t = 13$, together with 3-Gauss fits by red lines. Lower: 3-Gauss fits at $t = 12,\ 13,\ 14$.

TABLE V. 3-Gauss fit parameters at $t = 13$.

$V^{\mathcal{BB}}$	$\mathcal{V}_i$ (MeV)	ρ_i (fm)
$i = 0$	−491(60)	0.092(0.013)
$i = 1$	−254(64)	0.255(0.095)
$i = 2$	−110(144)	0.476(0.180)
$V^{\mathcal{BB}^*}$	$\mathcal{V}_i$ [MeV]	ρ_i [fm]
$i = 0$	302(38)	0.086(0.007)
$i = 1$	138(47)	0.289(0.090)
$i = 2$	170(65)	0.578(0.063)
$V^{\mathcal{B}^*\mathcal{B}}$	$\mathcal{V}_i$ [MeV]	ρ_i [fm]
$i = 0$	−109(17)	0.147(0.125)
$i = 1$	−61.1(16.2)	0.288(0.051)
$i = 2$	−9.27(4.95)	0.820(0.188)
$V^{\mathcal{B}^*\mathcal{B}^*}$	$\mathcal{V}_i$ [MeV]	ρ_i [fm]
$i = 0$	456(26)	0.181(0.005)
$i = 1$	−76.2(6.1)	0.657(0.043)
$i = 2$	−1.53(1.45)	1.385(0.099)

the $\mathcal{B}$ channel and thus an unitary S-matrix, as long as we take real E below the $\mathcal{B}^*$ threshold [31], as will be explicitly shown later. For the analysis, we employ the coupled-channel Lippmann-Schwinger equation to incorporate effects of virtual $\mathcal{B}^*$ to the scattering in the $\mathcal{B}$ channel, which indeed lead to sizable corrections to results obtained in the single-channel analysis without virtual $\mathcal{B}^*$ states.

2. Matrix inversion method for the Lippmann-Schwinger equation

The Lippmann-Schwinger (LS) equation for the T-matrix with the potential matrix reads

$$T^{\alpha\beta}(\mathbf{p}_W^\alpha, \mathbf{p}_W^\beta) = V^{\alpha\beta}(\mathbf{p}_W^\alpha, \mathbf{p}_W^\beta) + \sum_\gamma \int d^3\mathbf{k}\, V^{\alpha\gamma}(\mathbf{p}_W^\alpha, \mathbf{k}) \times \frac{1}{(W - E_{\text{th}}^\gamma) - \mathbf{k}^2/2\mu^\gamma + i\varepsilon} T^{\gamma\beta}(\mathbf{k}, \mathbf{p}_W^\beta), \tag{40}$$

where $p_W^\alpha = \sqrt{2\mu^\alpha(W - E_{\text{th}}^\alpha)}$ is the momentum calculated from the total energy W and $E_{\text{th}}^\alpha = M_1^\alpha + M_2^\alpha$ is a threshold energy for a channel α.

We have employed the matrix-inversion method [32] to solve the LS equation, approximating the momentum integral by a finite sum over Gaussian quadrature points. For the S-wave component in the partial wave expansion, the LS equation is reduced to

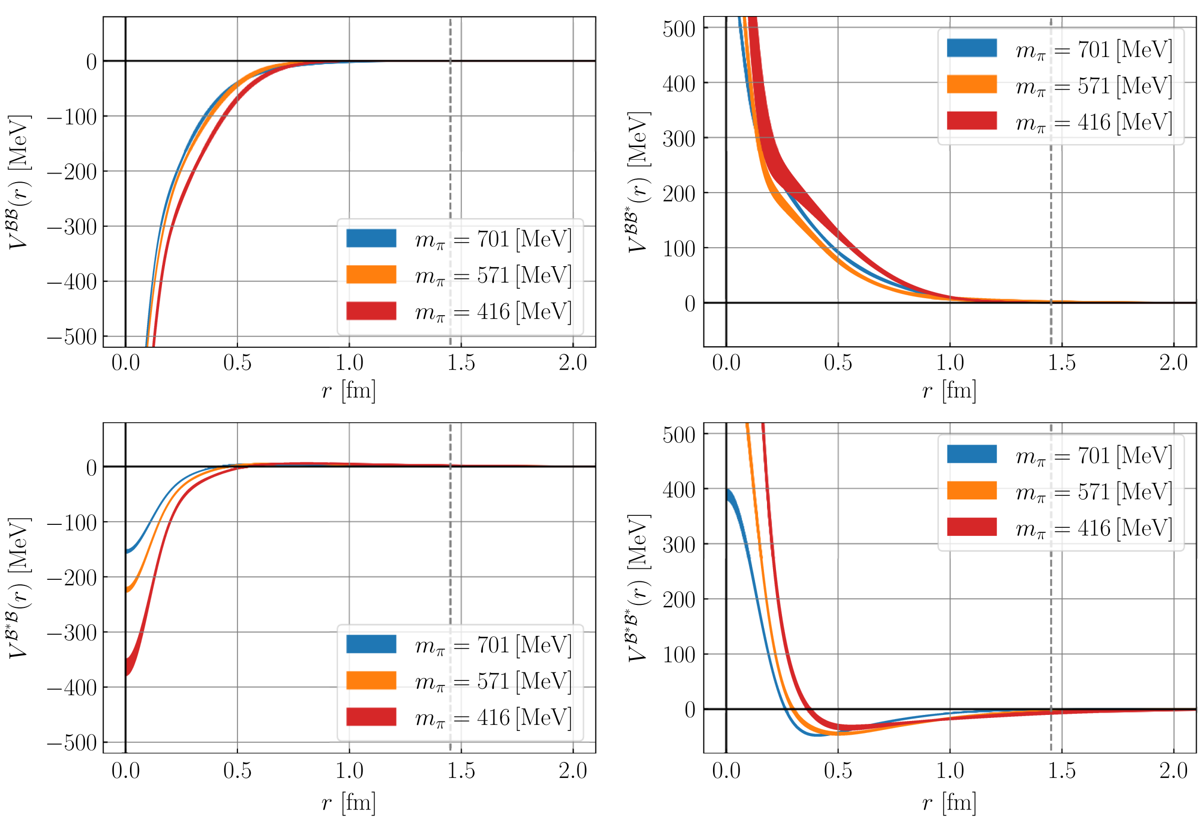

FIG. 3. Fit results $V_{3G}^{\alpha\beta}(r)$ at $m_\pi = 701$ MeV (blue), 571 MeV (orange), and 416 MeV (red) at $t = 13$.

$$t^{\alpha\beta}_{\ell=0}(k^\alpha_i, k^\beta_j) = \hat{V}^{\alpha\beta}_{\ell=0}(k^\alpha_i, k^\beta_j) - \sum_{\gamma,\delta}\sum_{m,n=0}^{N} \hat{V}^{\alpha\gamma}_{\ell=0}(k^\alpha_i, k_m)\hat{G}^{\gamma\delta}_0(k_m, k_n) \times t^{\delta\beta}_{\ell=0}(k_n, k^\beta_j), \tag{41}$$

where k_s with $s = 0, \ldots, N-1$ represents a momentum at the Gaussian quadrature point, while the on shell momentum p^α_W is stored in k^α_N. A matrix element of the potential for a Gaussian expansion of the potential, $V(r) = \sum_k \mathcal{V}_k e^{-r^2/\rho_k^2}$, is defined as

$$\hat{V}^{\alpha\beta}_0(k^\alpha_i, k^\beta_j) \equiv \frac{1}{\sqrt{4\pi}}\sqrt{\frac{\mu^\alpha\mu^\beta}{k^\alpha_i k^\beta_j}}\sum_k \mathcal{V}_k\rho_k \exp\left[-\frac{1}{4}\rho_i^2(k^\alpha_i + k^\beta_j)^2\right] \times (\exp[\rho_k^2 k^\alpha_i k^\beta_j] - 1), \tag{42}$$

while the Green function is given by

$$\hat{G}^{\gamma\delta}_0(k_m, k_n) \equiv \delta^{\delta\gamma}\delta_{mn} \times \begin{cases} \tilde{w}_m \frac{2k_m}{k_m^2 - 2\mu^\gamma(W - E^\gamma_{\text{th}})} & (m = 0, \ldots, N-1) \\ -\sum_{l=0}^{N-1}\tilde{w}_l \frac{2k^\gamma_N}{k_l^2 - 2\mu^\gamma(W - E^\gamma_{\text{th}})} + \mathrm{i}\pi & (m = N) \end{cases}, \tag{43}$$

where

$$k_j = p_{\text{cut}}\tan\left[\frac{\pi}{4}(x_j + 1)\right],$$
$$\tilde{w}_j = p_{\text{cut}}\frac{\pi}{4}\frac{w_j}{\cos^2\left[\frac{\pi}{4}(x_j+1)\right]}, \qquad x_j \in [-1, 1] \tag{44}$$

with the weight $w_j = \frac{2}{(1-x_j^2)[P'_N(x_j)]^2}$ for the Gauss-Legendre quadrature used in our calculations. We have confirmed that physical observables are insensitive to our choice, $N = 50$ and $p_{\text{cut}} = 100$ MeV. (Results are unchanged within errors for $p_{\text{cut}} = 1000$ MeV or $N = 60$.) Then, the T-matrix is approximately obtained by a matrix inversion as $t_0 = (\mathbf{1} - VG_0)^{-1}V$, where $t^{\alpha\beta}_0(k^\alpha_N, k^\beta_N)$ corresponds to the on shell T-matrix $t^{\alpha\beta}_0(W)$.

3. T-matrix and bound states

The scattering phase shift can be extracted from the on-shell T-matrix as

$$\frac{t^{\mathcal{BB}}_0(W)}{p^{\mathcal{B}}_W} = \frac{-1}{\pi}\frac{1}{p^{\mathcal{B}}_W\cot\delta^{\mathcal{BB}}_0(W) - ip^{\mathcal{B}}_W}, \tag{45}$$

and then $p\cot\delta$ is parametrized by the effective range expansion (ERE) as

$$p^{\mathcal{B}}_W\cot\delta^{\mathcal{BB}}_0(W) = -\frac{1}{a_0} + \frac{r_{\text{eff},0}}{2}(p^{\mathcal{B}}_W)^2 + \mathcal{O}((p^{\mathcal{B}}_W)^4), \tag{46}$$

where a_0 is the scattering length and $r_{\text{eff},0}$ is the effective range.

Since bound states correspond to poles of the T-matrix in a negative $(p^{\mathcal{B}}_W)^2$ axis, we have to solve the LS equation at $(p^{\mathcal{B}}_W)^2 < 0$ in order to find such poles. Alternatively, using (46), we may search an intersection between the ERE $p\cot\delta$ and a bound-state condition $-\sqrt{-p^2}$ at $(p^{\mathcal{B}}_W)^2 < 0$, which gives a pole at $p = +ip_{\text{BS}}$ in the upper-half complex $p^{\mathcal{B}}_W$ plane. In addition, for a pole of a physical bound state, $p\cot\delta$ must cross $-\sqrt{-p^2}$ from below as [33]

$$\frac{\mathrm{d}}{\mathrm{d}p^2}\left[p\cot\delta(p) - \left(-\sqrt{-p^2}\right)\right]\Big|_{p^2=-p^2_{\text{BS}}} < 0. \tag{47}$$

4. Results

Figure 4 shows scattering phase shifts as function of the energy from the $\mathcal{B}$ threshold ($W - m_B - m_{B^*}$) at $m_\pi \simeq 701$ MeV (upper left), 571 MeV (upper right), and 416 MeV (lower left), obtained below the $\mathcal{B}^*$ threshold but by the coupled-channel analysis. Physical phase shifts δ are calculated in the scattering region at $0 < W - M_B - M_{B^*} < W - 2M_{B^*} \simeq 45$ MeV, while bound states are examined at $W - M_B - M_{B^*} < 0$ using the analyticity of the S-matrix. As mentioned before, a bound state appears at the intersection between $p\cot\delta$ (pink, orange, red lines) and $-\sqrt{-p^2}$ (blue lines). It is observed that the system produces a pole of the T-matrix at each pion mass, which satisfies a physical pole condition, Eq. (47), so that one physical bound state exists at each pion mass. The thick line drawn along $-\sqrt{-p^2}$ curve is the binding energy independently obtained from the Schrödinger equation by the Gaussian expansion method (GEM) [34], which is consistent with the pole from the intersection. Here we set a number of bases of the GEM to 50 and the range parameters were set to be a geometric sequence with $b_1 = 100$ [1/fm^2] and $b_{50} = 0.0348$ [1/fm^2].

Figure 5 compares the binding energy obtained by the GEM in the coupled-channel analysis (cyan) with the one in the single-channel analysis (magenta) as a function of m_π^2 (open circles), together with a linear extrapolation in m_π^2 to the physical-pion mass $m_\pi = 140$ MeV (solid line), which predicts the binding energy at the physical pion mass as

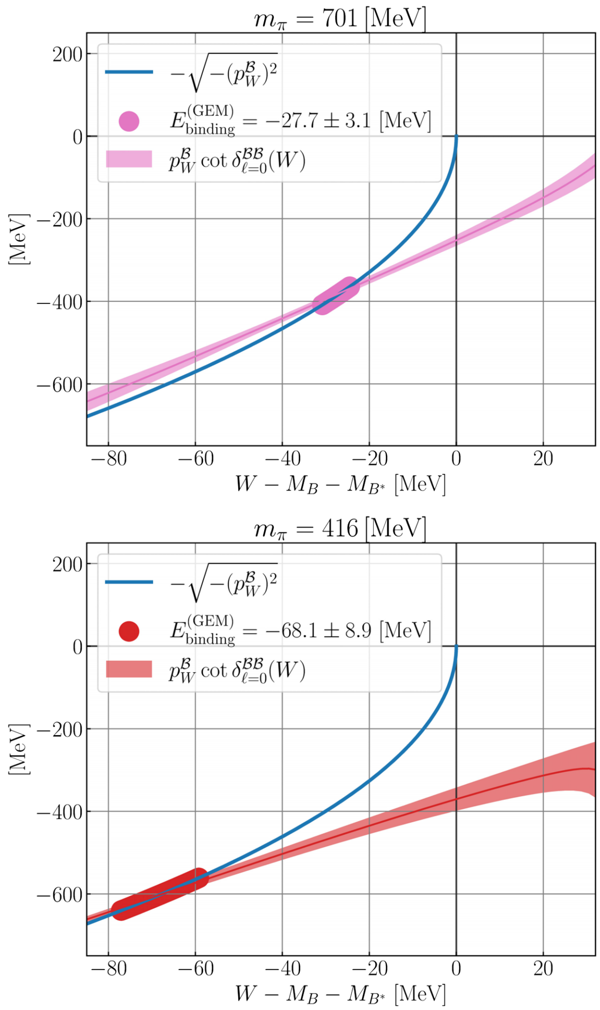

FIG. 4. Results of $p \cot \delta(W)$ from the LS equations as a function of $W < E_{\text{threshold}}^{\mathcal{B}^*}$, together with $-\sqrt{-p^2}$ by the blue solid line. A thick line along the $-\sqrt{-p^2}$ curve represents the binding energy calculated by the GEM, which agrees well with the intersection corresponding to a pole of the T-matrix.

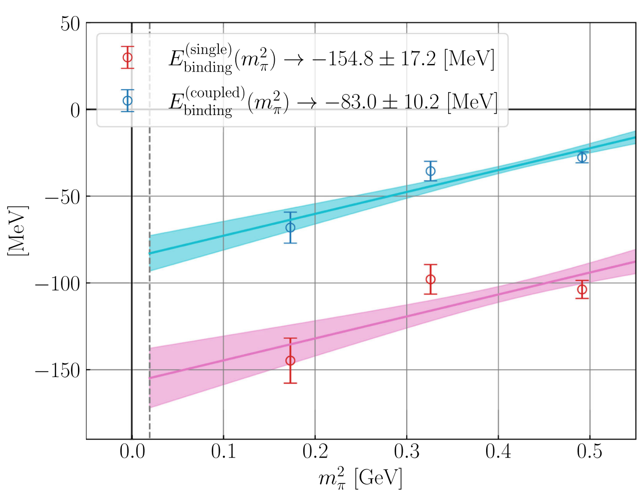

FIG. 5. The binding energy obtained by the GEM as a function of m_π^2 (open circles), together with a linear extrapolation in m_π^2 to $m_\pi = 140$ MeV (solid line) from the single-channel analysis (magenta) and the coupled-channel analysis (cyan).

$$E_{\text{binding}}^{(\text{single,phys})} = -154.8 \pm 17.2 \text{ MeV},$$
$$E_{\text{binding}}^{(\text{coupled,phys})} = -83.0 \pm 10.2 \text{ MeV}, \tag{48}$$

where errors are statistical only. A comparison of two results shows an about 40–50% reduction of the binding energy from the single-channel analysis to the coupled-channel analysis, probably due to large off-diagonal components of potentials. Thus, this systematics is attributed to virtual transitions such that $\mathcal{B} \to \mathcal{B}^* \to \mathcal{B}$, which may easily occur since the $\mathcal{B}^*$ threshold is only 45 MeV above the $\mathcal{B}$ threshold. Therefore, an inclusion of virtual $\mathcal{B}^*$ effect is required to predict physical observables such as the binding energy of the tetraquark state T_{bb} accurately in lattice QCD.

Figure 6 shows the scattering length a_0 (left) and the effective range $r_{\text{eff},0}$ (right) in the coupled-channel analysis, obtained from the ERE fit (46), as a function of m_π^2 (open circles), together with a linear extrapolation in m_π^2 to the

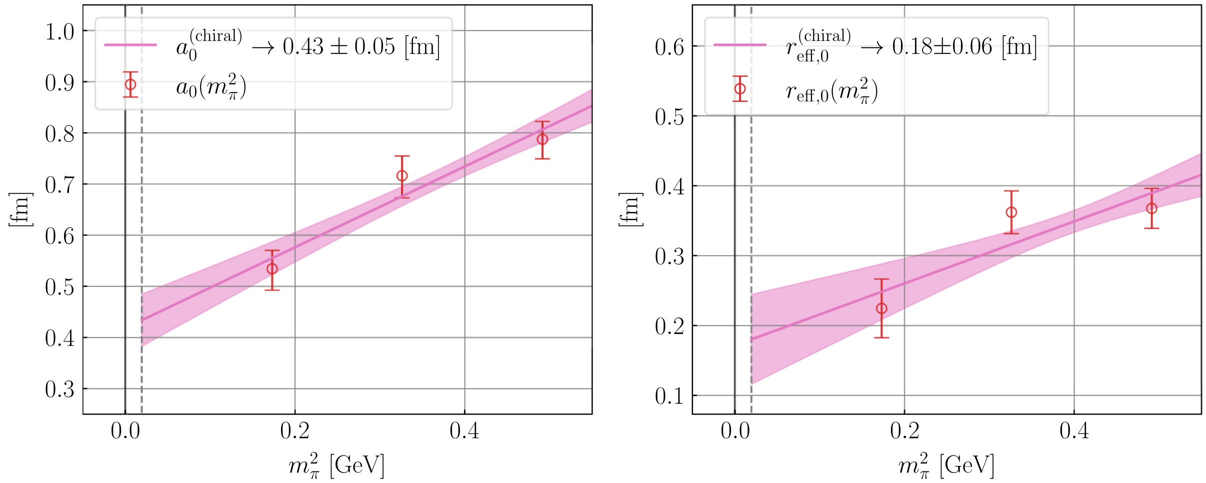

FIG. 6. ERE parameters in the coupled-channel analysis as a function of m_π^2 (open circles), together with a linear extrapolation in m_π^2 to $m_\pi = 140$ MeV (solid line). Left: the scattering length a_0. Right: the effective range $r_{\mathrm{eff},0}$. Both are defined in Eq. (46).

physical pion mass $m_\pi = 140$ MeV (solid line), which leads to

$$a_0^{(\mathrm{coupled,phys})} = 0.43 \pm 0.05\ \mathrm{fm},$$
$$r_{\mathrm{eff},0}^{(\mathrm{coupled,phys})} = 0.18 \pm 0.06\ \mathrm{fm}, \tag{49}$$

at the physical pion mass, where errors are again statistical only.

In Fig. 7, the binding energy at the physical pion mass is alternatively estimated from an intersection between

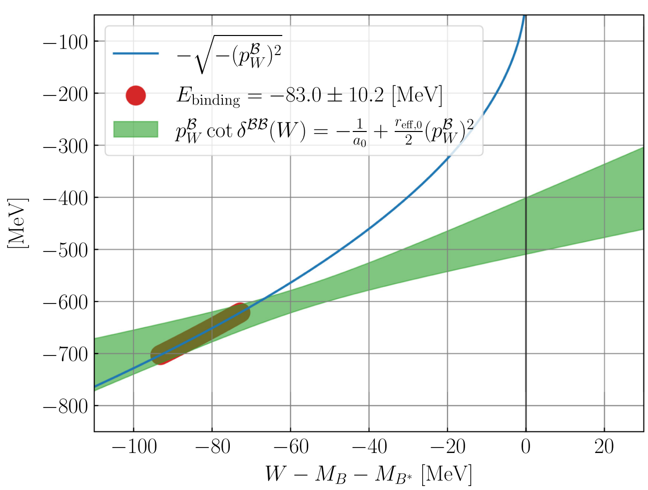

FIG. 7. The ERE at $m_\pi = 140$ MeV obtained with a_0 and $r_{\mathrm{eff},0}$ by linear extrapolations in m_π^2 (green band), together with $-\sqrt{-p^2}$ (blue solid line). An intersection of the two give a pole of the T-matrix, whose position is consistent with the binding energy by the GEM at $m_\pi = 140$ MeV by a linear extrapolations in m_π^2 (red thick curve along $-\sqrt{-p^2}$).

$-\sqrt{-p^2}$ (blue solid line) and $p\cot\delta(p)$ (green band) with $a_0^{(\mathrm{coupled,phys})}$ and $r_{\mathrm{eff},0}^{(\mathrm{coupled,phys})}$ in (49), which not only satisfies the physical-pole condition (47) but also well agrees with the binding energy by the GEM extrapolated directly to the physical pion mass (red thick curve along $-\sqrt{-p^2}$). The agreement in the binding energy between the two methods provide a strong support for reliability of our analysis.

V. CONCLUSIONS

In this paper, we have extracted scattering quantities through S-wave potentials between $\bar{B}$ and $\bar{B}^*$ mesons with quantum numbers $I(J^P) = 0(1^+)$, applying the coupled channel HAL QCD method to this single-channel scattering. We have employed the NRQCD action for b quarks to incorporate effects of their propagations in space. This paper presents the first analysis from a combination of the NRQCD action with the HAL QCD method. Physical observables such as the binding energy, the scattering length, and the effective range obtained on $(2+1)$-flavor full QCD configurations at three pion masses are extrapolated to the physical-pion mass.

Since off-diagonal potentials are asymmetric and comparable in magnitude to diagonal ones, as shown in Fig. 2, we have employed non-Hermitian 2×2 potentials in order to include the nonlocality caused by virtual $\mathcal{B}^*$ states into a single-channel potential as $U_{\mathrm{eff}}^{\mathcal{BB}}$. The single-channel analysis with $U_{\mathrm{eff}}^{\mathcal{BB}}$ show that the system with $\bar{B}$ and $\bar{B}^*$ mesons have a bound state corresponding to a doubly bottom tetraquark T_{bb}, whose binding energy is smaller by 40–50% than the one from the standard single channel analysis without nonlocality. This explicitly demonstrates an importance of virtual transitions between $\mathcal{B}$ and $\mathcal{B}^*$ channels to the tetraquark state T_{bb}. Thus, it may give some

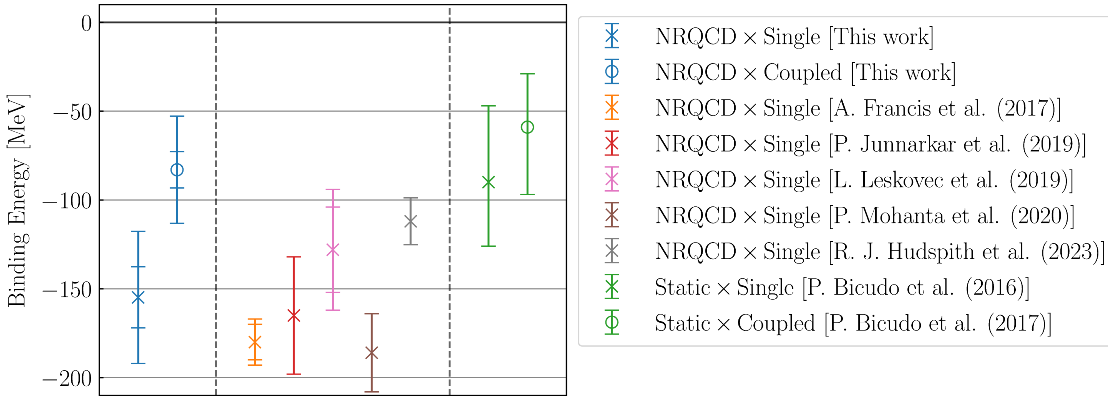

FIG. 8. A comparison of binding energies for the tetraquark bound state T_{bb} among several lattice QCD calculations, from the HAL QCD potential with the NRQCD b quark (blue symbols), spectra with the NRQCD b quark (squares), and the static-quark potential with the static b quark (green symbols). Crosses indicate results from the single-channel analysis, while open circles from the coupled-channel analysis.

hints on the nature of the tetraquark state T_{bb} such as its internal structure.

In addition to statistical errors quoted in Eqs. (48) and (49), we here estimate systematic errors in our result, which are caused by a truncation of the NRQCD expansion, a truncation of the perturbative matching between the NRQCD Hamiltonian and QCD, the finite lattice spacing, the finite volume, and the chiral extrapolation in lattice QCD simulations, and so on. Since these systematic errors are difficult to evaluate explicitly and precisely, we focus our attention on errors associated with the NRQCD action for b quarks and employ previous studies [12,29,35] for rough estimations. Effects of these systematics on the binding energy may be about 20 MeV at most, and other systematic errors such as the finite-lattice spacing, the finite volume and the chiral extrapolation are probably much smaller than 20 MeV, and thus are included in this 20 MeV. We then obtain

$$E_{\rm binding}^{(\rm single,phys)} = -154.8 \pm 17.2 \pm 20\ \text{MeV},$$
$$E_{\rm binding}^{(\rm coupled,phys)} = -83.0 \pm 10.2 \pm 20\ \text{MeV}, \tag{50}$$

for the final estimate of the binding energy including systematic errors.

We compare these final results with latest lattice studies [8–14] in Fig. 8. From the comparison, we draw following conclusions:

(i) In both cases of static quark potential and HAL QCD potential, the binding energies of T_{bb} in the coupled-channel analysis are smaller than those in the single-channel analysis. The reduction is larger for the HAL QCD potential; 155 MeV (blue cross) reduces to 83 MeV (blue open circle) for the HAL QCD potential, while 90 MeV (green cross) becomes 59 MeV (open circle) for the static-quark potential. Binding energies themselves are larger for the HAL QCD potentials than for the static-quark potentials in both single- and coupled-channel analyses. The moving b quarks in the NRQCD are probably responsible for this enhancement of binding energies.

(ii) Within the NRQCD b quark, our result in the single channel analysis (blue cross) roughly agrees with the direct-spectrum calculations (squares) within errors, though the systematic error of our result is large.

(iii) The result with the NRQCD b quark in the coupled-channel analysis (blue open circle) may be regarded as the best estimate of T_{bb}'s binding energy in this paper. While errors are large, the value, 83(10)(20) MeV, seems a little smaller than results from the NRQCD, ranging from 112(13) MeV to 186(22) MeV. To give a definite conclusion on this point, however, it will be necessary to reduce statistical as well as systematic errors in the HAL QCD method, for example, by improving the chiral extrapolation and performing the continuum extrapolation with a more precise NRQCD action.

While an existence a tetraquark bound state T_{bb} is a robust prediction in lattice QCD, reductions of systematic errors will be needed to evaluate its binding energy more precisely in future studies. A possible improvement is to extract T_{bb} spectra from correlations functions using optimized operators obtained by the HAL QCD potential [36].

ACKNOWLEDGMENTS

We thank the PACS-CS Collaboration [30] and ILDG/JLDG [37] for providing us their gauge configurations. We have used lattice QCD code of `Bridge++` [38], gauge-fixing code of `cuLGT` [39] and HAL QCD analysis is based on the code written by Dr. T. Miyamoto. In particular, we would like to thank Dr. H. Matsufuru, who has ported NRQCD code into the `Bridge++`.

Our numerical calculation was performed on Yukawa-21 at Yukawa Institute for Theoretical Physics (YITP) in Kyoto University. We thank other members of the HAL Collaboration, especially Dr. Y. Akahoshi, Mr. K. Murakami, and Dr. H. Nemura for fruitful discussions. This work is supported in part by the JSPS Grants-in-Aid for Scientific Research (No. JP16H03978, No. JP18H05236, and No. JP18K03628).

[1] R. Aaij *et al.* (LHCb Collaboration), Phys. Rev. D **102**, 112003 (2020).
[2] R. Aaij *et al.* (LHCb Collaboration), Nat. Phys. **18**, 751 (2022).
[3] R. Aaij *et al.* (LHCb Collaboration), Phys. Rev. Lett. **115**, 072001 (2015).
[4] A. Bondar *et al.* (Belle Collaboration), Phys. Rev. Lett. **108**, 122001 (2012).
[5] J.-B. Cheng, S.-Y. Li, Y.-R. Liu, Z.-G. Si, and T. Yao, Chin. Phys. C **45**, 043102 (2021).
[6] M. Karliner and J. L. Rosner, Phys. Rev. Lett. **119**, 202001 (2017).
[7] E. J. Eichten and C. Quigg, Phys. Rev. Lett. **119**, 202002 (2017).
[8] P. Bicudo, K. Cichy, A. Peters, and M. Wagner, Phys. Rev. D **93**, 034501 (2016).
[9] P. Bicudo, J. Scheunert, and M. Wagner, Phys. Rev. D **95**, 034502 (2017).
[10] A. Francis, R. J. Hudspith, R. Lewis, and K. Maltman, Phys. Rev. Lett. **118**, 142001 (2017).
[11] P. Junnarkar, N. Mathur, and M. Padmanath, Phys. Rev. D **99**, 034507 (2019).
[12] L. Leskovec, S. Meinel, M. Pflaumer, and M. Wagner, Phys. Rev. D **100**, 014503 (2019).
[13] P. Mohanta and S. Basak, Phys. Rev. D **102**, 094516 (2020).
[14] R. J. Hudspith and D. Mohler, Phys. Rev. D **107**, 114510 (2023).
[15] S. Aoki, N. Ishii, T. Doi, Y. Ikeda, and T. Inoue, Phys. Rev. D **88**, 014036 (2013).
[16] M. Luscher, Nucl. Phys. **B354**, 531 (1991).
[17] N. Ishii, S. Aoki, and T. Hatsuda, Phys. Rev. Lett. **99**, 022001 (2007).
[18] S. Aoki, T. Hatsuda, and N. Ishii, Prog. Theor. Phys. **123**, 89 (2010).
[19] S. Aoki, T. Doi, T. Hatsuda, Y. Ikeda, T. Inoue, N. Ishii, K. Murano, H. Nemura, and K. Sasaki (HAL QCD Collaboration), Prog. Theor. Exp. Phys. **2012**, 01A105 (2012).
[20] S. Aoki, N. Ishii, T. Doi, T. Hatsuda, Y. Ikeda, T. Inoue, K. Murano, H. Nemura, and K. Sasaki (HAL QCD Collaboration), Proc. Jpn. Acad. Ser. B **87**, 509 (2011).
[21] S. Aoki, B. Charron, T. Doi, T. Hatsuda, T. Inoue, and N. Ishii, Phys. Rev. D **87**, 034512 (2013).
[22] N. Ishii, S. Aoki, T. Doi, T. Hatsuda, Y. Ikeda, T. Inoue, K. Murano, H. Nemura, and K. Sasaki (HAL QCD Collaboration), Phys. Lett. B **712**, 437 (2012).
[23] J. R. Taylor, *The Quantum Theory of Nonrelativistic Collisions* (Dover books, New York, 1983).
[24] P. A. Zyla *et al.* (Particle Data Group), Prog. Theor. Exp. Phys. **2020**, 083C01 (2020).
[25] B. A. Thacker and G. P. Lepage, Phys. Rev. D **43**, 196 (1991).
[26] L. L. Foldy and S. A. Wouthuysen, Phys. Rev. **78**, 29 (1950).
[27] S. Tani, Prog. Theor. Phys. **6**, 267 (1951).
[28] G. P. Lepage, L. Magnea, C. Nakhleh, U. Magnea, and K. Hornbostel, Phys. Rev. D **46**, 4052 (1992).
[29] K.-I. Ishikawa, H. Matsufuru, T. Onogi, N. Yamada, and S. Hashimoto, Phys. Rev. D **56**, 7028 (1997).
[30] S. Aoki *et al.* (PACS-CS Collaboration), Phys. Rev. D **79**, 034503 (2009).
[31] S. Aoki, T. Iritani, and K. Yazaki, Prog. Theor. Exp. Phys. **2020**, 023B03 (2020).
[32] M. I. Haftel and F. Tabakin, Nucl. Phys. **A158**, 1 (1970).
[33] T. Iritani, S. Aoki, T. Doi, T. Hatsuda, Y. Ikeda, T. Inoue, N. Ishii, H. Nemura, and K. Sasaki, Phys. Rev. D **96**, 034521 (2017).
[34] M. Kamimura, Phys. Rev. A **38**, 621 (1988).
[35] S. Hashimoto, K.-I. Ishikawa, H. Matsufuru, T. Onogi, and N. Yamada, Phys. Rev. D **58**, 014502 (1998).
[36] Y. Lyu, H. Tong, T. Sugiura, S. Aoki, T. Doi, T. Hatsuda, J. Meng, and T. Miyamoto, Phys. Rev. D **105**, 074512 (2022).
[37] T. Amagasa *et al.*, J. Phys. Conf. Ser. **664**, 042058 (2015).
[38] S. Ueda, S. Aoki, T. Aoyama, K. Kanaya, H. Matsufuru, S. Motoki, Y. Namekawa, H. Nemura, Y. Taniguchi, and N. Ukita, J. Phys. Conf. Ser. **523**, 012046 (2014).
[39] H. Vogt and M. Schröck, in *GPU Computing in High-Energy Physics* (2015), pp. 175–180, arXiv:1412.3655.